# MALAYSIAN Journal of Catalysis

Vol. 9, No. 2, 2025 eISSN 0128-2581

**Topics of journal (but are not limited to):**

**1. Catalytic Mechanisms**
1-1. Spectroscopic and Visualizing Characterizations
1-2. Surface Chemistry, Reaction Kinetics and Mechanisms
1-3. Molecular Simulation and Theoretical Modeling
1-4. New Concepts for Catalysis

**2. Catalytic Materials**
2-1. Nanostructured Catalytic Materials
2-2. Micro- and Meso-Porous Catalytic Materials
2-3. Hybrid materials for catalysis

2-4. Novel Design and Synthetic Approaches

**3. Catalysis for Energy**
3-1. Efficient Utilization of Fossil Sources
3-2. Clean Energy Conversion: Electrocatalysis
3-3. Biomass Conversion
3-4. Photocatalysis for Hydrogen Production

**4. Environmental Catalysis**
4-1. Automotive Exhaust Cleanup
4-2. Water Pollution Control
4-3. Air Pollution Control
4-4. Updating and Utilization of Wastes

**5. Catalysis for Chemical Synthesis**
5-1. Green Synthesis
5-2. Petrochemicals
5-3. Fine Chemicals and Pharmaceuticals
5-4. Selective Oxidation & Hydrogenation

**6. Cross-Disciplinary**
6-1. Integration of Heterogeneous and Homogeneous
6-2. Organic and Biomimetic Catalysis
6-3. Industrial Catalysis
6-4. Other Surface Active Site Phenomena
6-5. Adsorption-Desorption Phenomena
6-6. Active sites Studies
6-7. Others



Faculty of Chemical and Energy Engineering
Universiti Teknologi Malaysia
http:/mjcat.utm.my/

Malaysian Journal of Catalysis
http://mjcat.utm.my/
MJCat
Research Article

# Z-Scheme CoPi/$Ag_3PO_4$ via Microwave Irradiation for Photodegradation of Rhodamine B

M.S. Azami[1*], N.H. Idris[1], A.H. Nordin[1], K.H. Tan[2], N. Jamaluddin[3], N.I.H. Hazril[4], N.M. Izzudin[4], A.A. Azmi[3]

[1]*Faculty of Applied Sciences, Universiti Teknologi MARA, 02600 Shah Arau, Perlis, Malaysia*
[2]*Centre for Advanced Materials, Faculty of Engineering and Technology, Tunku Abdul Rahman University of Management and Technology, 53300 Kuala Lumpur, Malaysia*
[3]*Faculty of Science, Universiti Teknologi Malaysia, 81310 UTM Johor Bahru, Johor, Malaysia*
[4]*School of Chemical and Energy Engineering, Faculty of Engineering, Universiti Teknologi Malaysia, 81310 UTM Johor Bahru, Johor, Malaysia.*
[5]*UTM Ocean Thermal Energy Centre, Universiti Teknologi Malaysia, Kuala Lumpur 54100, Malaysia*

**Corresponding Author: Tel: +601161717937 (saifulddin@uitm.edu.my)*

***Article history:***
*Received 24 December 2025*
*Accepted 26 December 2025*

**ABSTRACT**

The widespread use of synthetic dyes in the textile industry has led to severe water pollution, as most dyes are not firmly bound to fabrics and are released into aquatic ecosystems. Unchecked release of untreated dye-bearing effluents critically risks environmental quality and human health. Photocatalytic degradation is considered one of the best and most eco-friendly methods employed to degrade dye pollutants from wastewater. In the present study, a Z-scheme photocatalyst, cobalt phosphate (CoPi) and silver phosphate ($Ag_3PO_4$), abbreviated as CoPi/$Ag_3PO_4$, was synthesized by a microwave irradiation method for the photodegradation of Rhodamine B (RhB) dye under visible light. The as-synthesized photocatalysts were characterized by field emission scanning electron microscopy (FESEM), Fourier-transform infrared spectroscopy (FTIR), and UV-visible diffuse reflectance spectroscopy (UV-Vis DRS). The photocatalytic activity was evaluated using a dosage of 0.375 g/L of catalyst in irradiation for 60 minutes. The 5% CoPi/$Ag_3PO_4$ showed the highest degradation efficiency at 96%, followed by 10% CoPi/$Ag_3PO_4$ (92%), $Ag_3PO_4$ alone (87%), 1% CoPi/$Ag_3PO_4$ (82%), 15% CoPi/$Ag_3PO_4$ (73%), and CoPi alone (71%). The enhanced activity of 5% CoPi/$Ag_3PO_4$ was explained in terms of the homogeneous distribution of the Co and P elements on $Ag_3PO_4$ and the reduced band gap, which favors better absorption and separation of light. Further studies on the effect of different operating conditions, including initial pH, RhB concentration, and catalyst dosage, were conducted. The optimal degradation was achieved at pH 9, 10 mg/L of RhB, and a catalyst dosage of 0.375 g/L. Scavenger experiments indicated that photogenerated holes ($h^+$) were the major contributors to the mechanism of degradation. Finally, microwave-assisted CoPi/$Ag_3PO_4$ synthesis is a simple and efficient route to produce visible-light-responsive photocatalysts. Doping CoPi significantly enhanced the photocatalytic activity of $Ag_3PO_4$, and the composite is a promising material for the degradation of dye-contaminated wastewater

*Keywords*: *Z-scheme, Photocatalyst, Rhodamine B, Microwave, Silver Phosphate*


| eISSN 0128-2581 |

## 1. INTRODUCTION

Rhodamine B (RhB) is a xenobiotic group of carcinogens in the body and can increase free radicals. It contains chlorine compounds (Cl-), the $CH_3$-$CH_3$, the aromatic micro carbon polycyclic (PAH) Activates the cytochrome enzyme P-450 as well as the very redox structure of the quinone and cause the formation of Reactive Oxygen species (ROS) [1]. RhB waste disposal is a potential threat to marine and terrestrial species, as well as to humans. RhB exposure shortens the length of the estrous cycle in chatty adult females [2]. Follicle atresia and failure to develop can result from a disease called folliculogenesis. As was previously indicated, organic dyes have been subjected to a wide range of treatment strategies. Those techniques, however, have drawbacks like being time-consuming, expensive to produce, and able to produce by-products [3]. As a result, the use of semiconductor photocatalysts in the Advanced Oxidation Process (AOPs) to degrade RhB has attracted widespread attention as a potentially powerful destructive technique for eliminating RhB from the hydrosphere. $Ag_3PO_4$'s narrow band gap and low valence band level make it an effective photocatalyst for oxidizing pollutants. Despite its useful features, $Ag_3PO_4$ has low photostability because photogenerated electron-hole pairs quickly recombine and Ag ions are rapidly reduced to metallic Ag in the presence of light [4]. Numerous solutions,

such as introducing composite coupling with other semiconductors, have been proposed to address this problem. Composite photocatalysts have the potential to enhance photocatalyst stability, inhibit electron-hole pair recombination, enhance charge carrier separation, and lower surface redox reaction activation energies [5].

According to its abundance on Earth, low cost, photocatalytic properties, and small band gap (2.0 eV), corresponding to the visible light range, cobalt phosphate, CoPi, has recently garnered significant attention from researchers. In addition, some research has shown that adding CoPi to a photocatalyst significantly enhances its ability to oxidize water [6]. To further boost its photocatalytic efficiency, this photocatalyst can also function as a hole collector, reducing the rate at which electron-hole pairs recombine. CoPi/$Ag_3PO_4$ was first synthesized by Geng et al.,[6] utilizing a one-step hydrothermal process. CoPi/$Ag_3PO_4$ composite preparation using the traditional approach required at least 24 hours for each sample. This effort will focus on creating a CoPi/$Ag_3PO_4$ composite photocatalyst employing microwave irradiation for the photodegradation of RhB dye in light of this problem. No investigations on the manufacture of CoPi/$Ag_3PO_4$ utilizing microwave irradiation, which makes it possible to produce the composite photocatalyst with a quick reaction time and low energy input, have previously been described in the scientific literature [7].

## 2. EXPERIMENTS

### 2.1 Preparation of Cobalt Phosphate

The preparation of cobalt phosphate, CoPi, was prepared using the precipitation method. 0.5 g of disodium ammonium phosphate dibasic ($(NH_4)_2HPO_4$) was dissolved in 10 mL of distilled water (solution A). Meanwhile, 1.5 g of cobalt nitrate hydrate $Co(NO_3)_2xH_2O$. $Co(NO_3)_2xH_2O$. was dissolved in 40 mL of distilled water, and the solution was continuously stirred for 30 min (solution B). Solution A was mixed with solution B and stirred for 2 hours. Then, the red precipitation was collected and dried for 4 hours at 110 ℃.

### 2.2 Preparation of Silver Phosphate

The preparation of silver phosphate ($Ag_3PO_4$) was prepared using the precipitation method. 0.5 g of disodium hydrogen phosphate anhydrous ($Na_2HPO_4$) was dissolved in 10 mL of distilled water (solution A). Meanwhile, 1.5 g of silver nitrate ($AgNO_3$) was dissolved in 40 mL of distilled water with continuous stirring for 30 min (solution B). Solution A was mixed with solution B and stirred for 2 hours. Then, the yellow precipitation was collected and dried for 4 hours at 110 ℃.

### 2.3 Synthesis of CoPi/$Ag_3PO_4$

The facile solid-state method under microwave irradiation was used to prepare the composite catalyst of CoPi/$Ag_3PO_4$. The appropriate amount of CoPi and $Ag_3PO_4$ was mixed in 50 Ml of distilled water. The mixed catalyst was dried for 2 hours at 110 ℃. The dry yellow solid was placed in the microwave for 30 min at 450 W. The CoPi weight loading in the range between 1-15 wt. % were investigated and denoted as x- CP/AP, specifically as 1 CP/AP, 5, CP/AP, 10 CP/AP, and 15 CP/AP.

### 2.4 Photocatalytic degradation of RhB

The photocatalytic performance of the prepared photocatalysts was compared based on the photodegradation of RhB under visible light irradiation. Photodegradation activity was carried out by suspending 0.03 g of photocatalyst in 25 mL of an aqueous 0.3 mM solution of RhB. This suspension was poured into a glass cell of dimensions 50 mm width × 10 depth × 80 height and irradiated with a 20 W white color LED lamp of irradiance 237 W m-2 with a wavelength between 200-380 nm. An aquarium pump model NS 7200 was used as an aeration source for the supply of oxygen. During each photocatalytic experiment, the decolorization of RhB was determined at specific time intervals until a steady state. The absorbance was measured using an HACH DR 1900 spectrophotometer at 554 nm.

### 2.5 Characterization

The microscopic surface morphology of the prepared photocatalysts was evaluated through a field-emission scanning electron microscope (FESEM). The optical absorbance was recorded via ultraviolet-visible/diffuse reflectance spectra (UV-Vis/DRS) spectrophotometer and the extrapolation of bandgap photocatalysts. The chemical functional group of the photocatalyst was measured using Fourier transform infrared (FTIR) via the KBr method.

## 3. RESULTS AND DISCUSSION

### 3.1 Characterization of photocatalysts

#### 3.1.1 Vibrational spectroscopy

In this study, XRD analysis was performed with the range of 2θ=5- 50° for Al-MCM-41 and 2θ=5-80° for Ni/Al-MCM-41. The diffraction pattern of Al-MCM-41 and Ni/Al-MCM-41 were shown in Figure 1 dan Figure 2. The characteristic peak of the Al-MCM-41 material may be seen in the diffractogram of the material at 2θ=15–30°. This peak suggests the presence of an amorphous phase in the Al-MCM-41 material [20,21]. The impregnated Ni on Al-MCM-41 catalyst exhibits additional peaks at 2θ= 37°, 43°, 62°, and 75° which are associated with the diffraction planes (111), (210) (220), and (311) of face-centered cubic NiO

[22,23]. The presence of the characteristic NiO peak shows that NiO was impregnated successfully on the surface of Al-MCM-41 [4].

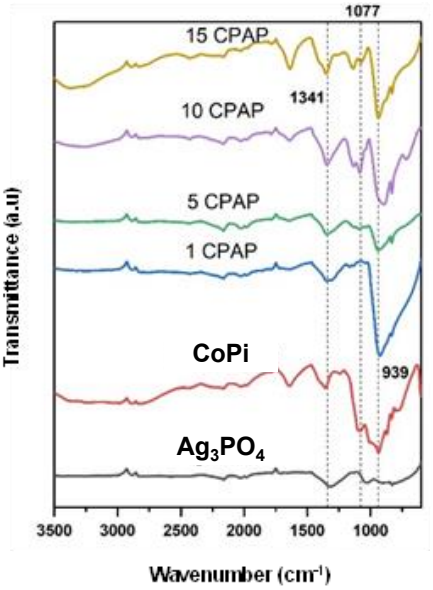


**Figure 1.** FTIR spectra of synthesized $Ag_3PO_4$, CoPi, 1 CP/AP, 5 CP/AP, 10 CP/AP and 15 CP/AP with band spectra at 600 – 3500 $cm^{-1}$

### 3.1.2 Morphological studies

The surface morphological nature of the prepared photocatalysts was analysed by FESEM micrographs and the recorded images are shown in Figure 2. From the FESEM micrograph, it can be seen that the prepared pure CoPi shows flake-like morphology, while pure $Ag_3PO_4$ exhibited an irregular shape, as depicted in Figure 2b. The 5 CP/AP sample displays irregular spherical morphology. It was also observed that two components CoPi and $Ag_3PO_4$, were dispersed well in the hybrids. The well-distributed elements contacted from CoPi on the surface of $Ag_3PO_4$ are predicted to harvest more visible light that can be absorbed during photocatalytic degradation.

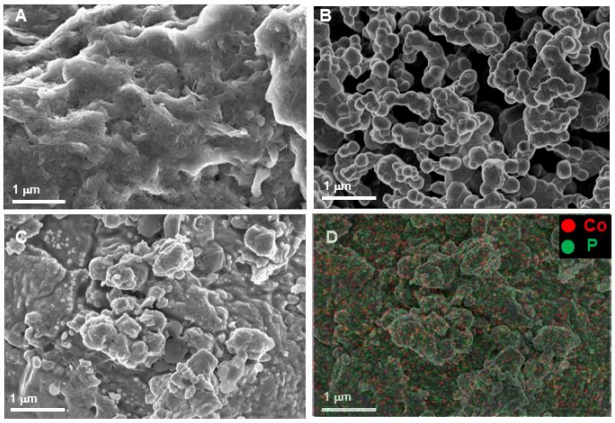


**Figure 2.** FESEM image of sample (a) CoPi (b) $Ag_3PO_4$ (c) 5 CPAP, (d) Elemental mapping of sample 5 CPAP showing the spatial presence of Co and P

### 3.1.3 Optical property studies

The pyridine adsorption FTIR was used to determine the number and kind of acid sites on the catalyst. The pyridine-FTIR spectra of all samples show three adsorption peaks at 1446, 1490 and 1546 $cm^{-1}$ which correlated to Lewis and Brønsted acid sites [25,26]. The adsorption peak at 1446 $cm^{-1}$ was generated due to the transferring electron pairs from the secondary amine group in pyridine to Lewis acid sites in the catalyst. Meanwhile, adsorption at 1546 $cm^{-1}$ correspond to proton transfer from Brønsted acid sites to form a pyridinium ion ($C_5H_5NH^+$) with a pyridine molecule [27]. The adsorption peak at wave number 1490 $cm^{-1}$ associated to the total peak of both Lewis acid and Brønsted acid sites.

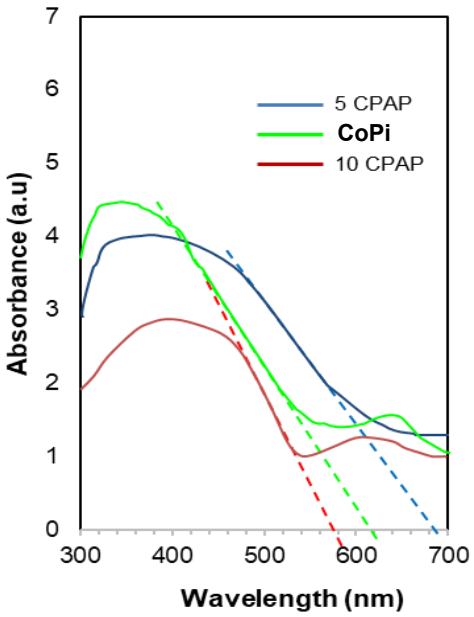


**Figure 3.** UV-vis diffuse reflectance spectra of the prepared photocatalyst

### 3.2 Photocatalytic degradation of RhB

The photodegradation of Rhodamine B (RhB) under visible light was used to determine the photocatalytic activity of CP/AP. In order to compare, the identical conditions were used to study the activities of pure CoPi and $Ag_3PO_4$. As depicted in the Figure 4, when compared to pure CoPi and $Ag_3PO_4$, all CP/AP catalysts exhibit a greater photocatalytic degradation rate. Since $Ag_3PO_4$ acts as a supporting catalyst, the composites with CoPi doped in proportions ranging from 1% to 15% demonstrate that the photocatalytic activity differs depending on the ratio. The results of a 60-minute investigation into the CP/AP catalysts'

photocatalytic activity in the breakdown of RhB are illustrated in Figure 4. Evidently, 5 CP/AP degraded at the highest rate (96%) followed by 10 CP/AP (92%), $Ag_3PO_4$ (87%), 15 CP/AP (73%) and CoPi (71%). The highest performance of 5 CP/AP is owing to the well-distribution element of Co and P on the $Ag_3PO_4$, which led to high interaction between these two catalysts and reduced band gap energy that will generate more active site and improve the interfacial charge transfer [11].

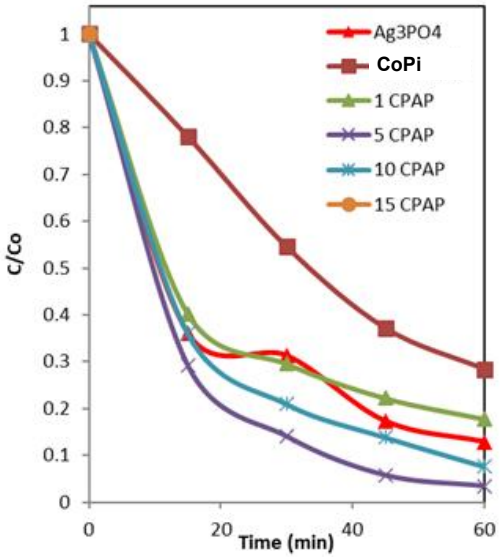


**Figure 4.** Photodegradation of RhB under visible-light irradiation for the prepared photocatalysts ([RhB] = 10 mg $L^{-1}$, pH = 6, [catalyst] = 0.0250 g $L^{-1}$, t = 1 h, 30 ºC)

## 3.3 Photocatalytic degradation mechanism

Next, the effect of scavenger was performed to determine the role of scavenger species in the photocatalytic mechanism of RhB over 5 CP/AP is shown in Figure 5. The experiment was carried out by using Potassium Iodide (PI), Isopropanol (IP), Methanol (ME) and Potassium Chlorate (PC) as scavenger species for absorbed on the catalyst ($•OH_{surface}$), photogenerated hydroxyl radicals absorbed in the bulk solution ($•OH_{bulk}$) photogenerated holes ($h^+$) and photogenerated electrons (e-), respectively [12]. Noticeably, Figure 5 indicates that the photogenerated $h^+$ (66%) played the most crucial role in the photocatalytic decomposition of RhB, followed by photogenerated $•OH_{surface}$ bulk (70%), and $•OH_{bulk}$ (85%). In contrast, the inactive species for 5 CP/AP are photogenerated e- (94%). The above results verified that the interdependent interaction.

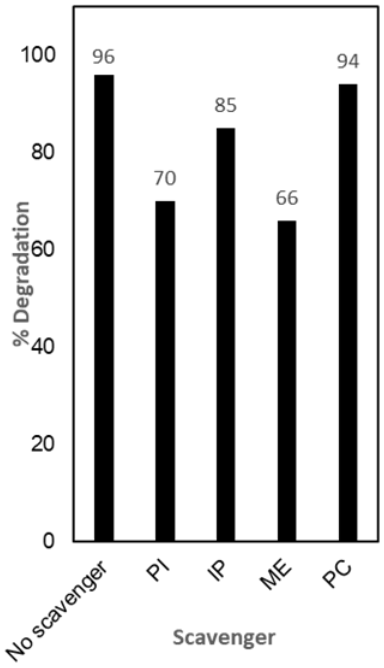


**Figure 5.** Effect on Scavenger on photodegradation of RhB using 5 CP/AP photocatalyst ([RhB] = 10 mg $L^{-1}$, pH = 6, [catalyst] = 0.0250 g $L^{-1}$, t = 1 h, 30 ºC)

Based on the above analysis and discussion, a potential Z-Scheme mechanism of the CP/AP photocatalyst was proposed and schematically illustrated in Figure 6. As the bandgap energy of $Ag_3PO_4$ has been established in earlier studies [13], it was not re-evaluated here; instead, the reported bandgap value was 2.42 eV, which was used for VB and CB calculations in this proposed mechanism..The photogenerated electrons in the CB of $Ag_3PO_4$ will recombine with the photogenerated holes in the VB of CoPi, separating the holes in the VB of $Ag_3PO_4$ and the electrons in the CB of CoPi. Because of its greater negative redox potential than $O_2/•O_2^-$, the electrons in the CB of CoPi have a potential of -0.38 eV, which can create $•O_2^-$. While the holes in the VB of $Ag_3PO_4$ have a potential of 2.65 eV, they can oxidize $H_2O$ to produce •OH radical because their redox potential is much more positive than the potential level of $H_2O/•OH$ (2.44 eV). Both •OH and $h^+$ are active radicals that can continually destroy RhB. The internal electric field created by the potent interface between CoPi and $Ag_3PO_4$ can speed up the recombination of photogenerated electrons in the CB of $Ag_3PO_4$and photogenerated holes in the VB of CoPi. The effective Z-scheme heterostructure preserved with superior oxidic-ability is credited with superior photocatalytic performance.

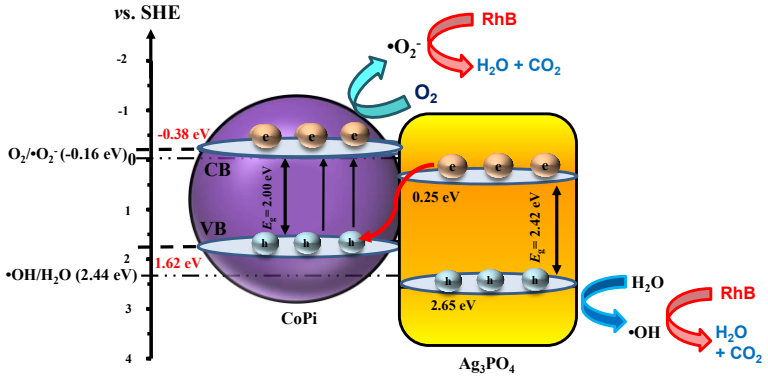


**Figure 6.** Mechanism of photocatalytic activity of composite CPAP photocatalyst

## 4. CONCLUSION

In this study, a remarkable enhancement of photocatalytic capability under visible light irradiation was achieved by forming a bulk heterojunction containing CoPi and $Ag_3PO_4$. This enhancement was ascribed to the efficient charge separation at the heterojunction built between $Ag_3PO_4$ and CoPi. It is observed that 5 CP/AP serve as the best photocatalyst for degradation of RhB under visible light, with the highest percentage degradation compared to pure $Ag_3PO_4$ and pure CoPi. The physical and chemical properties of the photocatalysts were examined using FTIR, UV-Vis DRS and FESEM analyses. The results of the characterization show that CoPi was well dispersed on the surface of the $Ag_3PO_4$. Hence, the bandgap of 5 CP/AP was the lowest compared to others. In addition, 5% CoPi loaded with $Ag_3PO_4$ shows to be greatly effective in enhancing the photodegradation of RhB activity as compared to pure CoPi, $Ag_3PO_4$, 1 CP/AP, 5 CP/AP, 10 CP/AP, and 15 CP/AP. This suggests that 5 CP/AP has the best performance in photodegradation of RhB due to its well-dispersed, strong interaction between Co, P and Ag bonds and lowest bandgap. Moreover, the effect of the scavenger shows that the photogenerated $h^+$ (66%) played the most crucial role in the photocatalytic decomposition of RhB. Then, the mechanism for the photocatalytic activity of RhB was proposed as a Z-Scheme heterojunction. Overall, the CoPi loaded on $Ag_3PO_4$ successfully contribute on photodegradation of RhB under visible light.

## ACKNOWLEDGEMENTS

The authors are grateful for the financial support from the Fundamental Research Grant Scheme- Early Career from the Ministry of Higher Education Malaysia (Grant No. 600-RMC/FRGS-EC 5/3 (056/2024) @ FRGS-EC/1/2024/STG04/UITM/02/16) and Kurita Water and Environment Foundation Research Grant Program 2023 (grant number 4J652).

## REFERENCES

1. D. R. Sulistina, S. Martini, Energy Sources, Journal of Public Health Research **9(2)** (2020) 101-104.
2. H. Rohmawati, M. E. Fitriasnani, W. T. Purnani, R. K. Dewi, Journal of Physics: Conference Series **899(1)** (2021).
3. Q. Liu, IOP Conference Series: Earth and Environmental Science **514(5)** (2020).
4. M. S. Azami, A. A.Jalil, F. F. A. Aziz, N. S. Hassan, C. R. Mamat, , A. A. Fauzi, N. M. Izzudin, Separation and Purification Technology, **292** (2022) 120984.
5. A. Amirulsyafiee, M. M. Khan, M. H. Harunsani, Catalysis Communications **172** (2022) 106556.
6. Z. Geng, M. Yang, X. Qi, Z. Li, X. Yang, M. Huo, J. C. Crittenden, Journal of Chemical Technology & Biotechnology **94(5)** (2019) 1660–1669.
7. Q. Hu, Y. He, F. Wang, J. Wu, Z. Ci, L. Chen, R. Xu, M. Yang, J. Lin, L. Han, D. Zhang, Chinese Medicine **16(1)** (2021) 1–22.
8. S. Mandal, R. Ananthakrishnan, ACS Sustainable Chemistry and Engineering **6(1)** (2018) 1091–1104.
9. W. Shi, M . Li, X. Huang, H. Ren, C. Yan, F. Guo, Chemical Engineering Journal 382(2020) 122960.
10. X. Li, , P. Xu, M. Chen, G. Zeng, D. Wang, F. Chen, W. Tang, C. Chen, C. Zhang, X. Tan, Chemical Engineering Journal **366** (2019) 339–357.
11. O.M. Halim, H. Haslinda, , Z. Ahmad, W.I Nawawi, K.H. Tan, Jamaluddin, N, Izzudin, N.M., Jalil, A.A, Azmi, A.A. and Azami, M.S. Malaysian Journal of Chemistry **7(3)** (2025) 38-47.
12. W. Shi, C. Liu, M. Li, X. Lin, F. Guo, J. Shi, Journal of Hazardous Materials 389 (2020).
13. M. S. Azami, A. A. Jalil, W. I. Nawawi, C. R. Mamat, N. M. Izzudin, Materials Today: Proceedings **66(P10)** (2022) 4068–4072.

Malaysian Journal of Catalysis 9 (2025) 54-57

Malaysian Journal of Catalysis
http://mjcat.utm.my/

MJCat
Research Article

# Epoxidation of Cooking Oil Using Natural Zeolite as Heterogeneous Catalyst Via Peracids Mechanism

Muhammad Akhiruddin Zainal Abidin[1], Norin Hafizah Rahim[1], Nur Aisyah Aleya Jamian[1], Mohd Jumain Jalil[1]*

[1]*Chemical Engineering Studies, College of Engineering, Universiti Teknologi MARA, Cawangan Johor, Kampus Pasir Gudang*

**Corresponding Author: mjumain0686@uitm.edu.my*

***Article history:***
*Received 24 December 2025*
*Accepted 30 December 2025*

**ABSTRACT**

The increasing demand for sustainable and environmentally friendly materials has directed attention towards the epoxidation of vegetable oils for biopolymer and plasticizer production. This study investigates the use of natural zeolite as a heterogeneous catalyst in the epoxidation of cooking oil via the in situ peracids mechanism. The epoxidation was carried out using hydrogen peroxide and formic acid at 80°C, with varying catalyst loadings to examine their effect on oxirane yield and reaction kinetics. The oxirane oxygen content (OOC) was monitored through titration, while Fourier Transform Infrared Spectroscopy (FTIR) confirmed structural changes in the oil. Results showed that 0.25 g of natural zeolite yielded the highest relative conversion to oxirane (RCO) of 68.6% within 10 minutes, with higher catalyst amounts resulting in lower efficiency due to possible side reactions. FTIR analysis revealed the successful conversion of unsaturated fatty acids into epoxides, as indicated by the disappearance of alkene (C=C) peaks and the appearance of epoxy (C-O-C) peaks. The study confirms the catalytic potential of natural zeolite as a greener and reusable alternative to conventional homogeneous catalysts, supporting sustainable practices in bio-based chemical processes.

*Keywords*: *Epoxidation, corn oil, oxirane ring, kinetic study*


| eISSN 0128-2581 |

## 1. INTRODUCTION

The epoxidation of cooking oil has become a crucial step in the production of bio-based materials, offering sustainable alternatives to petroleum-derived products. As global industries increasingly focus on environmentally friendly practices, the demand for efficient and green chemical processes has never been greater [1]. According to Wai *et al.* [2], epoxidized vegetable oils play a vital role in the production of plasticizers, stabilizers, and biopolymers. It also contributes significantly to reducing the reliance on non-renewable resources. The catalyst selection is important to this process performance since it directly influences reaction efficiency, product yield, and environmental impact [3]. Sulfuric acid, a widely used homogeneous catalyst, offers high reactivity but poses challenges such as product contamination and separation difficulty. On the other hand, heterogeneous catalysts like natural zeolite provide recyclability and reduced contamination risks, aligning with sustainable production goals [4] [5].

In the epoxidation of oils, catalyst efficiency plays a vital role in optimizing conversion rates and ensuring sustainable industrial applications. The use of natural zeolite as a heterogenous catalyst in the epoxidation of vegetable oils has been explored extensively due to its eco-friendly and reusable nature. The findings journals demonstrated the effectiveness of natural zeolite in the in situ epoxidation of oleic acid, highlighting its catalytic activity in promoting high epoxide yields under mild reaction conditions [5]. Furthermore, natural zeolite not only facilitates cleaner production methods but also offers enhanced sustainability by minimizing the generation of harmful by-products [6]. The catalytic reaction in the epoxidation process using natural zeolite and sulphuric acid as a catalyst has been studied to understand their different benefits and mechanisms [7]. Natural zeolite, a heterogeneous catalyst, improves reaction efficiency and is environmentally friendly because it can be reused and is not corrosive [8]. On the other hand, sulphuric acid is a homogeneous catalyst, was found to be highly effective and produce better epoxide yields, but it is corrosive and creates waste that needs careful disposal [9]. The comparison for both types of catalyst found that natural zeolite is better for the environment and reusable, while sulphuric acid works faster under specific conditions [10].

Despite extensive studies on natural zeolite as a heterogeneous catalyst for vegetable oil epoxidation, the effect of catalyst loading on oxirane formation under in situ

peracid conditions remains insufficiently explored. Therefore, this study investigates the epoxidation of cooking oil using natural zeolite with hydrogen peroxide and formic acid. The influence of catalyst loading on oxirane yield and reaction performance is evaluated, while FTIR analysis is used to confirm epoxy ring formation.

Overall, natural zeolite is more sustainable and eco-friendly option compared to sulphuric acid. The choice of catalysts, which affects reaction efficiency, selectivity and sustainability, has a big impact on this problem. Homogeneous catalysts, such as sulphuric acid, are typically used as due to their high catalytic activity. However, their use is associated with challenges, such as environmental issues, difficulties in separation, and product contamination. On the other hand, heterogeneous catalysts, such as natural zeolites provide benefits including lower contamination risks, ease of separation, and reusability which are align with sustainable industrial practices [11][12].

## 2. EXPERIMENTS

### 2.1 Materials

Cooking oil that we use for this study is palm oil from EcoSafa. The Oxidising agent is 30- 32% hydrogen peroxide brand from Chemiz. The oxygen carrier is 85% formic acid brand from Chemiz, and the acetic acid is 100% glacial brand from Chemiz. In titration process and boost its efficiency, catalysts such sulphuric acid 96–97% brand from Chemiz, and catalyst of NaOH and HCl is used for this process. For the titration procedure, this process used crystal violet and hydrogen bromide 48-50% brand from Chemiz.

### 2.2 Epoxidation method

The process began by preparing a water bath on a hot plate to maintain consistent reaction conditions as shown in Figure 1. A measured amount of 50 g of cooking oil was mixed with Hydrogen Peroxide and Formic Acid with the molar ratio 1:1:1. A magnetic stirrer was added to ensure the mixture was well blended, and the beaker was set in the water bath, with the temperature maintained at 80°C and stirring at 350 rpm for uniformity. In this experiment the temperature and stirring need to be monitored to make sure it maintained at 80°C and stirring at 350 rpm to monitor the progress, samples were taken every 10 minutes, mixed with hydrogen bromide, and analyzed through titration to measure the oxirane content. This step helped assess the reaction's effectiveness and the impact of different catalyst concentrations.

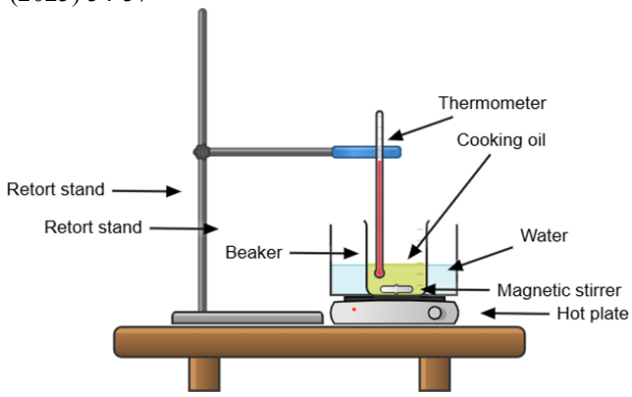


**Figure 1.** Apparatus set up for epoxidation process

## 3. RESULTS AND DISCUSSION

### 3.1 Effect of Heterogeneous Catalyst (Natural Zeolite) in Cooking Oil Epoxidation

The data analysis for the epoxidation of cooking oil using natural zeolite as a heterogeneous catalyst focuses on evaluating the relative conversion to oxirane (RCO%) across varying catalyst weights (0.25 g, 0.50 g, 0.75 g and 1.0 g) and reaction times at (10 to 70 minutes). By analysing the experimental oxirane oxygen content (OOCexp) and compare it with theoretical oxirane oxygen content (OOCtheo), the reaction efficiency was determined. The optimal conditions were identified based on the maximum RCO achieved at specific catalyst weights and reaction time. This analysis provides insights into the catalytic performance of natural zeolite, assessing its efficiency in leading the epoxidation reaction and identifying the most effective catalyst concentration for achieving high conversion rates.

From Figure 2, the graph shows the relative conversion to oxirane (RCO%) over reaction time during the epoxidation of cooking oil using varying weights of natural zeolite catalysts weights at 0.25 g, 0.50 g, 0.75 g and 1.0 g. The results show that the catalyst weight significantly influences the reaction kinetics and conversion efficiency. For 0.25 g, the RCO% peaks at approximately 68.6% at 10 minutes, indicating that this is the optimal condition for maximum conversion. As for 0.50 g of natural zeolite catalyst that expressed in Figure 3.2, the RCO% reached a maximum of 68.16% at 10 minutes, showing the comparable initial performance but slightly lower conversion rates at extended reaction times. As for 0.75 g of natural zeolite catalyst, it resulted in a lower maximum RCO of 58.99% at 10 minutes, indicating that higher catalyst amounts might not enhance the reaction efficiency due to potential side reactions. Lastly, at 1.0 g of natural zeolite catalyst, the RCO peaked at 48.53% at 10 minutes and decreased consistently, suggest that excessive catalyst concentration might hinder the performance, that leads to produce the highest oxirane conversion at shortest reaction time.

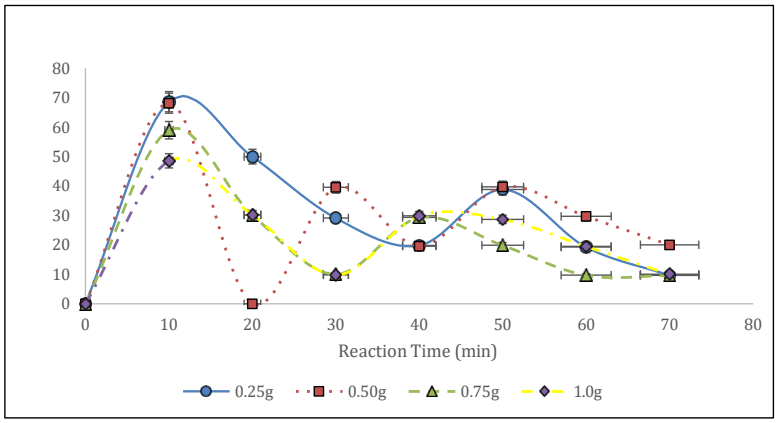


**Figure 2.** Relative conversion (RCO%) against reaction time (min) for epoxidation of cooking oil with natural zeolite catalyst

## 3.2 Fourier Transform Infrared Spectroscopy (FTIR)

The FTIR analysis helps in identify key functional groups and bonds that make up its framework. Natural zeolite is primarily composed of silica (Si) and alumina (Al) bonds, which form its unique porous structure. These features are crucial for its catalytic performance. The specific vibrations of bonds, such as Si-O-Si and Al-O-Si, which confirm the stability and functionality of the zeolite can be detect by analysing FTIR spectrum. Figure 3 shows the analysis of FTIR spectrum of raw cooking oil against epoxide cooking oil for natural zeolite catalyst.

The hydroxyl group (O-H) peak was observed in the range of (3200-3600 $cm^{-1}$) in both raw and epoxidized cooking oil. However, its intensity decreased in epoxidized oil, suggesting that some hydroxyl groups reacted with the epoxide during the reaction. This reduction aligns with previous findings that indicate a decrease in free fatty acids upon epoxidation [13]. The alkyl group (C-H) peak, detected between (2800-3000 $cm^{-1}$), remained strong in both raw and epoxidized oil, implying that the hydrocarbon backbone of the triglycerides remained intact. This result was expected since epoxidation primarily targets the (C=C) bonds rather than (C- H) bonds [14].

A key transformation was observed in the ester carbonyl group (C=O) at range (1700- 1750 $cm^{-1}$). In raw cooking oil, this peak was prominent due to the presence of triglycerides. However, a decrease in intensity was recorded in epoxidized oil, indicating that some ester groups underwent transformation, potentially due to secondary reactions with the epoxide ring [6].

The alkene (C=C) peak at (1600-1680 $cm^{-1}$) was strong in raw cooking oil but disappeared in epoxidized cooking oil. These disappearances confirms that the double bonds were successfully converted to epoxide groups, verifying the efficiency of the epoxidation process [15]. The formation of epoxy groups was validated by the epoxy (C-O-C) peak in the range of (850-1250 $cm^{-1}$), which was absent in raw cooking oil but appeared strongly in the epoxidized sample. The presence of this peak provides direct evidence of epoxidation, demonstrating the conversion of unsaturated fatty acids into oxirane rings [4].

Additionally, the role of natural zeolite catalyst was confirmed by the intensification of (Si-O-Si) range at (1000-1250 $cm^{-1}$) and (Al-O-Si) range at (450-900 $cm^{-1}$) peaks in epoxidized cooking oil. These peak indicate the interaction between the epoxide and zeolite framework, suggested that zeolite facilitated the reaction by providing an active surface for oxidation.. In summary, FTIR analysis confirms the successful conversion of unsaturated fatty acids into epoxides, as indicated by the disappearance of the (C=C) peak and the emergence of the (C-O- C) peak. The interaction between the oil and the zeolite catalyst is evidenced by changes in the (Si-O-Si) and (Al-O-Si) peaks. These findings support the effectiveness of natural zeolite as a catalyst in epoxidation reactions.

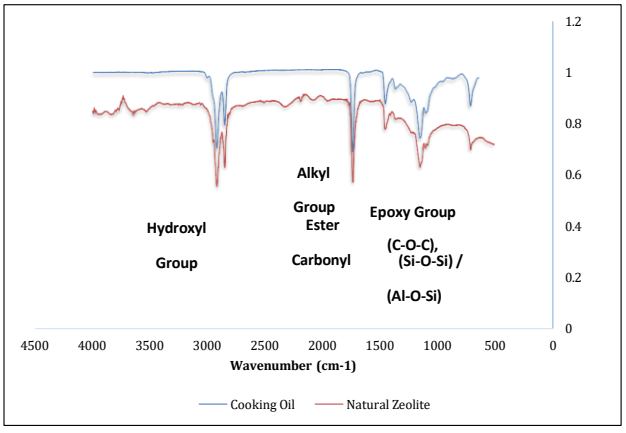


**Figure 3.** FTIR spectrum of raw cooking oil against epoxide cooking oil for natural zeolite catalyst

## 4. CONCLUSION

This study demonstrates that natural zeolite is an effective and sustainable heterogeneous catalyst for the epoxidation of cooking oil via the in situ peracids mechanism. Among the catalyst loadings tested, 0.25 g provided the highest oxirane conversion at the shortest reaction time, indicating an optimal balance between catalyst activity and reaction efficiency. FTIR analysis further confirmed the successful formation of oxirane rings and the transformation of unsaturated bonds in the oil. The findings highlight the environmental and practical advantages of using natural zeolite, including reusability, reduced contamination, and alignment with green chemistry principles. This work contributes to the advancement of eco-friendly epoxidation processes and supports the development of renewable resources for industrial applications.

## REFERENCES


1. N. Kamairudin, S. S. Hoong, L. C. Abdullah, H. Ariffin, and D. R. A. Biak, Molecules **26 (3)** (2021).
2. P. T. Wai, P. Jiang, Y. Shen, P. Zhang, Q. Gu, and Y. Leng, RSC Adv., 9 (65) (2019) 38119–38136.
3. N. Mohamed, I. S. Azmi, M. A. Riduan, N. I. A. Morsidi, N. Kamal, and M. J. Jalil, Int. J. Chem. React. Eng. (2025) 1–5.
4. M. Z. Mohd Yunus, S. K. Jamaludin, S. F. Abd Karim, A. Abd Gani, and A. Sauki, IOP Conf. Ser. Mater. Sci. Eng. **358 (1)** (2018).
5. I. S. Azmi, S. A. Adnan, A. N. Masri, S. D. Nurherdiana, S. N. Abdullah, and M. J. Jalil, Environ. Prog. Sustain. Energy **43 (4)** (2024).
6. M. Kurańska and M. Niemiec, Catalysts **10 (11)** (2020) 1–13.
7. J. D. Udonne, B. O. Alade, and R. J. Patinvoh, **7 (3)** (2016) 491–500.
8. N. D. Kasmin, I. S. Azmi, S. D. Nurherdiana, F. A. M. Yusof, and M. J. Jalil, Environ. Prog. Sustain. Energy, 43(5) (2024).
9. N. Mohamed, M. J. Jalii, S. K. Jamaludin, and A. R. M. Daud, J. Appl. Sci. Agric., 9 (11) (2014) 86–92.
10. M. J. Jalil, M. H. N. Ishak, I. M. Rasib, M. Z. A. Kadir, M. Noorfazlida, and I. S. Azmi, 73 (2024) 477–481.
11. M.J. Jalil, I. Izni, S. Erwan, H. Hamzah, R. Ismail, R. Siti, A. Intan, Environ. Prog. Sustain. Energy 44(2) (2025).
12. D. L. H. Maia and F. A. N. Fernandes, Biomass Convers. Biorefinery **12** (2020) 5861-5868.
13. Neswati and N. Nazir, IOP Conf. Ser. Earth Environ. Sci., 757(1) (2021) 012069.
14. S. Dworakowska, D. Bogdał, and A. Prociak, "Synthesis of polyols from rapeseed oil, 3–7.
15. M. Jumain, J. Intan, S. Azmi, A. Hadi, A. Farhan, and M. Yamin, J. Polym. Res. (2022) 1–12,

Malaysian Journal of Catalysis
http://mjcat.utm.my/
MJCat
Research Article

# Mesostructured $TiO_2$–g-$C_3N_4$ Hybrid Nanocomposites: A Potential Solar-Driven Solution for Textile Dye Pollution

Siti Munirah Sidik[1,2*], Mohamad Saufi Rosmi[1,2], Muhammad Shaiful Aidil Mohd Syarafuddin[1], Nurul Adilah Mohd Noor[1], Nur Farhana Jaafar[3], NurFatehah Wahyuny Che Jusoh[4], Wan Haslinda Wan Ahmad[1,2]

[1]*Department of Chemistry, Faculty of Science and Mathematics, Universiti Pendidikan Sultan Idris, 35900 Tanjong Malim, Perak, Malaysia*
[2]*Nanotechnology Research Center, Faculty of Science and Mathematics, Universiti Pendidikan Sultan Idris, 35900 Tanjong Malim, Perak, Malaysia*
[3]*School of Chemical Sciences, Universiti Sains Malaysia, 11800 Gelugor, Penang, Malaysia*
[4]*Malaysia Japan International Institute of Technology, Universiti Teknologi Malaysia, 54100 Kuala Lumpur, Malaysia*

**Corresponding Author: smunirah@fsmt.upsi.edu.my*

***Article history:***
*Received 24 December 2025*
*Accepted 30 December 2025*

**ABSTRACT**

The development of efficient solar-driven photocatalysts is crucial for sustainable treatment of dye-contaminated textile wastewater. In this study, a mesostructured titania/graphitic carbon nitride hybrid nanocomposite (MTNCN) was successfully synthesized via an impregnation method and evaluated for the photodegradation of methylene blue (MB) under UV and solar irradiation. The structural and physicochemical properties of the synthesized materials were systematically characterized using X-ray diffraction (XRD), field emission scanning electron microscopy with energy-dispersive X-ray analysis (FESEM–EDX), $N_2$ adsorption–desorption (BET) analysis, and UV–Vis diffuse reflectance spectroscopy (UV-Vis DRS). The XRD and FESEM–EDX results confirmed the successful incorporation and uniform distribution of CN into MTN, while preserving and enhancing the structural framework of MTN. The formation of an effective heterojunction in MTN–CN was found to enhance the textural and optical properties, significantly increasing the surface area and pore volume while reducing the particle size and band gap energy of the pristine MTN. In the photocatalytic activities, MTNCN demonstrated superior performance, achieving 78.2 % MB degradation within 30 min and 97.3 % after 180 min under solar irradiation, outperforming both pristine MTN and CN, even under UV light. This enhanced performance under solar irradiation underscores the strong potential of MTNCN as an efficient and sustainable photocatalyst for textile dye wastewater remediation.

*Keywords*: *mesostructured titania, graphitic carbon nitride, hybrid nanocomposite, solar-driven photocatalysis, methylene blue*


| eISSN 0128-2581 |

## 1. INTRODUCTION

The textile industry is one of the most water-intensive industrial sectors, generating large volumes of dye-containing wastewater during processes such as dyeing, printing, and finishing [1]. In Malaysia, where the textile sector contributes significantly to the national economy, the discharge of toxic and persistent coloured effluents poses serious threats to aquatic ecosystems, human health, and environmental sustainability [2]. Such effluents often exceed regulatory limits for key water quality parameters, including biochemical oxygen demand (BOD) and ammoniacal nitrogen [3], highlighting the urgent need for effective and sustainable wastewater treatment technologies.

Advanced oxidation processes (AOPs) have emerged as promising alternatives to conventional treatment methods due to their operational simplicity, cost-effectiveness, and ability to mineralize organic pollutants into harmless end products [4]. Among the tested catalysts, semiconductor-based photocatalysis has attracted considerable attention for wastewater remediation due to its ability to absorb light at suitable wavelengths and generate electron–hole pairs, which subsequently degrade pollutants via radical-mediated mechanisms [5]. Many semiconductors have been investigated as promising photocatalysts; however, among them, titania ($TiO_2$) remains the most widely used [6]. This material exhibits excellent chemical properties while being cost-effective, non-toxic, and chemically stable. Furthermore, owing to its ease of synthesis, key characteristics such as crystallinity, polymorphic composition, morphology, surface area, and particle size can be readily tailored [7].

To date, mesoporous titania nanoparticles (MTN) have shown potential as a photocatalysts owing to their high surface area, good crystallinity, and enhanced adsorption capacity. Previous study reported that MTN prepared under various aging time showed a potential as a photocatalyst in MB photodegradation [8]. However, their wide band gap (~3.2 eV) limits photoactivity to the ultraviolet (UV) region and is further hindered by rapid electron–hole recombination [9]. Graphitic carbon nitride (g-$C_3N_4$), a metal-free and chemically stable semiconductor with a narrower band gap (~2.7 eV), offers visible-light responsiveness and has been widely explored for photocatalytic applications [10]. Hybridizing MTN with g-$C_3N_4$ (CN) to form heterojunction nanocomposites is an effective strategy to enhance light absorption, improve charge separation, and boost overall photocatalytic performance.

In this study, MTNCN nanocomposites were synthesized via an impregnation method and evaluated for MB degradation under UV and simulated solar irradiation. The physicochemical properties of the photocatalysts were characterized using XRD, $N_2$ adsorption–desorption (BET) analysis, FESEM, and UV–Vis DRS.

## 2. EXPERIMENTS

### 2.1 Materials

Hexadecyltrimethyl-ammonium bromide (CTAB) and titanium (IV) isopropoxide (TTIP) were purchased from Sigma-Aldrich. Ammonium hydroxide ($NH_4OH$) and urea ($CH_4N_2O$) were purchased from Systerm and *n*-propanol was purchased from Bendosen. MB powder was purchased from Tunchem. All chemicals used in this research work were analytical grade and did not require any further purification.

### 2.2 Preparation of Catalysts

The MTN catalyst was synthesized using sol-gel method, reported earlier by [11] with some modifications. 4.68 g of CTAB surfactant was added into 720 mL distilled water, 120 mL *n*-propanol and 29 mL of 28 % ammonia solution. Then, the mixture was magnetically stirred for 30 min at 50 °C in a water bath. After 30 min, the temperature of water bath was increased to 80 °C before 5.7 mL of TTIP was added into the mixture. The solution was continued stirred for another 2 hours in water bath to allow the mixture dissolved completely. After 2 hours of stirring, the observed white solution was transferred into a container and placed in the refrigerator (5 °C) for 2 days. Then, the as-synthesized MTN solution was centrifuged at 4000 rpm to collect the gel product and dried overnight in oven at 100 °C. Finally, the product was calcined at 550 °C for 3 hours to remove the impurities.

The graphitic carbon nitride (CN) was usually synthesized using chemical route pioneered by [12]. In this study, 50 g of urea were mixed with 10 mL of distilled water and placed in a porcelain crucible with cover, and was subsequently calcined at 550 °C for 3 hours with heating rate of 2 °C/min in furnace under air atmosphere. After the calcination process, the furnace was allowed to cool to room temperature, resulting a pale-yellow powder.

The hybrid MTN and 1 wt. % CN was prepared by wet impregnation method and labelled as MTNCN. Firstly, 1 g of MTN was added to the mixture of 10 mL of distilled water and desired amount of urea (as the precursor of CN) before undergone the stirring process continuously for 10 min. After that, the mixture was placed in a porcelain crucible with cover, and was subsequently calcined at 550 °C for 3 hours with heating rate of 2 °C/min in furnace under air atmosphere. After the calcination process, the furnace was allowed to cool to room temperature.

### 2.3 Characterization of Mesoporous Titania Nanoparticles (MTN)

The prepared catalysts were then characterized by X-ray diffraction (XRD) analysis (Model: Rigaku MiniFlex) with Cu Kα radiation (λ = 1.5418 Å) at 2θ angle ranging from 20 ° to 80 °. The phases were identified with aid of the Joint Committee on Powder Diffraction Standards (JCPDS) library. The crystallite sizes of the synthesized catalyst were determined based on the major peak at $2\theta = 25.5$ ° using the Debye-Scherrer equation.

$$d = \frac{k\,\lambda}{\beta \cos\theta} \quad (1)$$

where $d$ is the crystallite size, $k$ is the shape factor ($k$ = 0.94), $\lambda$ is the wavelength of the X-ray radiation (Cu $K_\alpha$ = 0.1542 nm), $\beta$ is the line width at half-maximum height and $\theta$ is the diffraction angle at the peak maximum [9]. The morphological properties and elements of the catalysts were examined by field-emission scanning electron microscopy (FESEM) with energy dispersive x-ray (EDX) analysis (Model: Hitachi, SU 8020, UHR). The $N_2$ adsorption-desorption analysis (Model: SA 3100 Surface Analyzer Beckman Coulter) was performed by using the Brunauer-Emmett Teller (BET) method which could estimate the surface area, pore volume and pore size of the catalysts. Before measurement, all samples were degassed at 300 °C and 0.1 Pa. The band gaps were measured using a PerkinElmer Lambda 900 UV- Vis DRS spectrophotometer at 300 to 800 nm wavelengths.

### 2.4 Photodegradation of Methylene Blue (MB)

The photodegradation was performed when 0.1 g of catalyst was added into 100 mL of MB solution and constantly stirred in a 250 mL glass vessel. Before illumination, the solution was magnetically stirred for 30 min in the dark to achieve adsorption-desorption equilibrium. Then, the reaction was continued for another 180 min with irradiation of 400W LED UV lamp (395 nm)

under continuous stirring. During the reaction, 2 mL of aliquots were sampled every 30 min and centrifuged using a micro centrifuge at 13000 rpm for 30 min to separate the liquid phase from solid catalyst before being analyzed by UV-Visible (UV-Vis) spectroscopy (Model: Jasco V-570) at $\lambda_{max}$ = 665 nm [13]. The degradation percentage was calculated using the following equation;

$$\text{Degradation (\%)} = \left(\frac{C_o - C_t}{C_o}\right) \times 100 \quad (2)$$

where $C_o$ is the initial concentration of MB before being exposed to irradiation and $C_t$ is the concentration of MB at a specific time. The same procedure was repeated by changing the source of light irradiation to solar light.

## 3. RESULTS AND DISCUSSION

### 3.1 Physicochemical Properties of the Prepared MTN

Figure 1 showed the XRD pattern of CN, MTN and MTNCN. The XRD patterns of MTN and MTNCN showed a similar pattern with the presence of diffraction peaks at 2θ = 25.5, 38.2, 48.2, 54.3, 55.3, 63.1, 70.5, 70.7 and 75.7 ° are corresponding to the characteristic crystal planes of (101), (004), (200), (105), (211), (204), (116), (220) and (215) anatase phase, and matched well with JCPDS 21-1272 [14]. No diffraction peaks of the CN at 2θ = 27.3 ° corresponding to the (002) diffraction is detected on the MTNCN, probably due to the low loading and well distribution on the surface of the catalysts [13]. It also a noteworthy that the particle size of MTN was decreased after CN loadings from 12.44 nm to 11.80 nm, respectively.

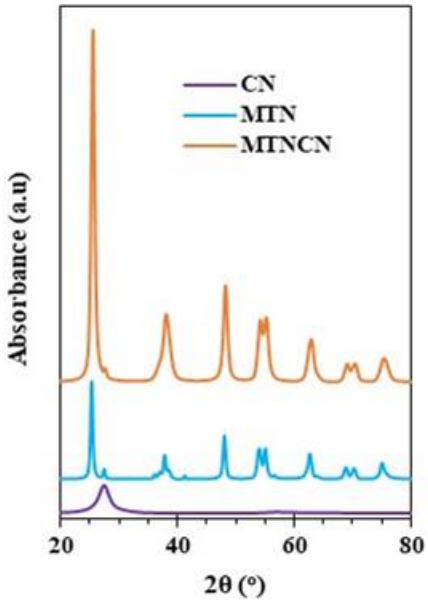


**Figure 1.** The XRD pattern of CN, MTN and MTNCN.

The morphology and surface characteristics of the MTNCN were demonstrated using FESEM, as illustrated in Figure 2. From the low magnification image (Figure 2 a, b), it can be seen that the MTNCN are in porous arrangement and formed abundance of deep narrow slits. A close-up image at higher magnifications (Figure 2 c, d) demonstrated that the MTNCN was made up from an aggregation of small spherical nanoparticles (less than 100 nm) forming a framework like structure with hole in the middle. This result is consistent with the morphology reported in the previous study [8], indicating that the incorporation of CN into MTN does not alter the framework structure of MTN. In fact, the increase in MTN diffraction peak intensities after CN introduction (as observed in Figure 1) suggests oriented grain growth during the incorporation of CN [15].

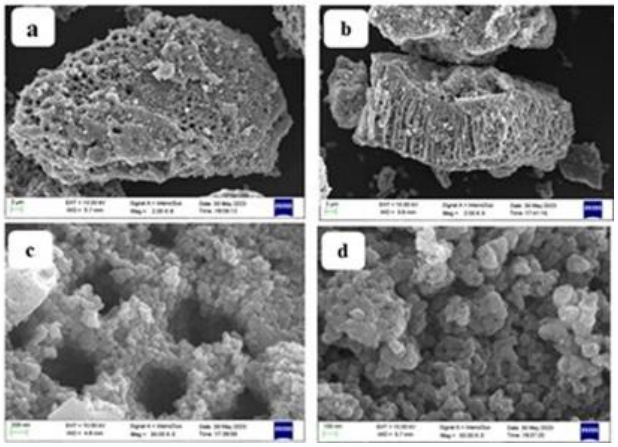


**Figure 2.** FESEM images of MTNCN at (a, b) 2,000, (c) 30,000 and (d) 50, 000 magnifications.

Further examination on the distribution of element on the surface of the catalyst was conducted by elemental mapping analysis, and results are shown in Figure 3.3 (a-f). Based on the analysis, there are four main elements were detected on the surface of the catalyst which is titanium (Ti), oxygen (O), nitrogen (N) and carbon (C), represented by different colored dots. The presence of uniformly distributed Ti, O, N and C elements indicated successful assembly of CN into MTN [16]. It can be observed that the signal intensity of Ti and O is much stronger than that of C and N. This phenomenon can be explained by the lower percent of CN in the MTNCN catalyst.

Table 3.1 summarizes the textural and optical properties of MTN, CN and MTNCN. According to $N_2$ adsorption–desorption (BET) results, the lowest surface area was found on MTN (28.66 $m^2/g$), followed by CN (37.49 $m^2/g$) and MTNCN (66.30 $m^2/g$). Specific surface areas and pore volume of the MTNCN is greater than those of CN and MTN, suggesting a significant quantity of CNs may promote a good dispersion of CNs in hybrids, which would benefit the expansion of certain surface areas and generation of new pores [17]. On the other hand, the pore size were decreased upon CN loading. This may be resulted from the deposition of CN particles in/on the surface of pores of the MTN, thus reducing the average pore size as compared to the MTN [18].

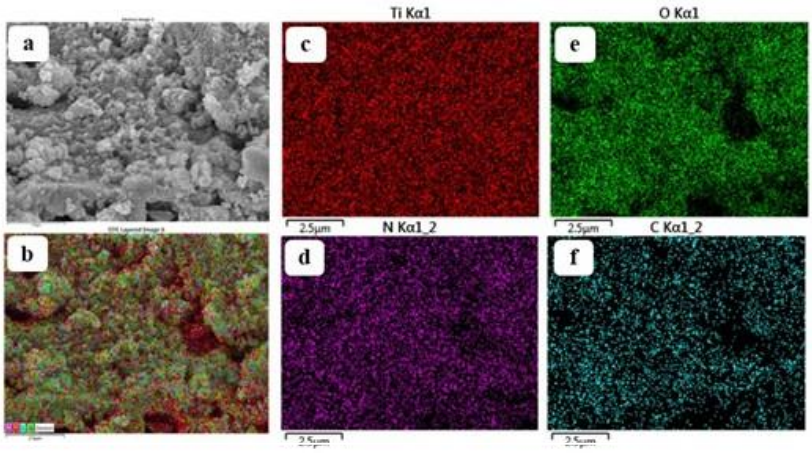


**Figure 3.** EDX images of (a) MTNCN, (b) multilayer (c) Ti, (d) N, (e) O, and (f) C elements.

**Table 1.** Textural and optical properties of MTN, CN and MTNCN 1%.

| Catalyst | [a]Surface Area ($m^2/g$) | [a]Pore volume ($cm^3/g$) | [a]Pore size ($cm^3/g$) | [b]Particle Size (nm) | [c]Band gap (eV) |
|---|---|---|---|---|---|
| MTN | 28.66 | 0.122 | 16.29 | 12.44 | 3.04 |
| CN | 37.49 | 0.100 | 13.18 | n.a | 2.74 |
| MTNCN | 66.30 | 0.182 | 11.17 | 11.80 | 2.94 |

[a] obtained from $N_2$ adsorption - desorption analysis using BET method.
[b] calculated using Scherer Equation using (101) peak at $2\theta = 25.5$ °
[c] determined form the plot of $[F(R)hv^{(0.5)}]$ versus photon energy (hv) using Kubelka-Munk calculation

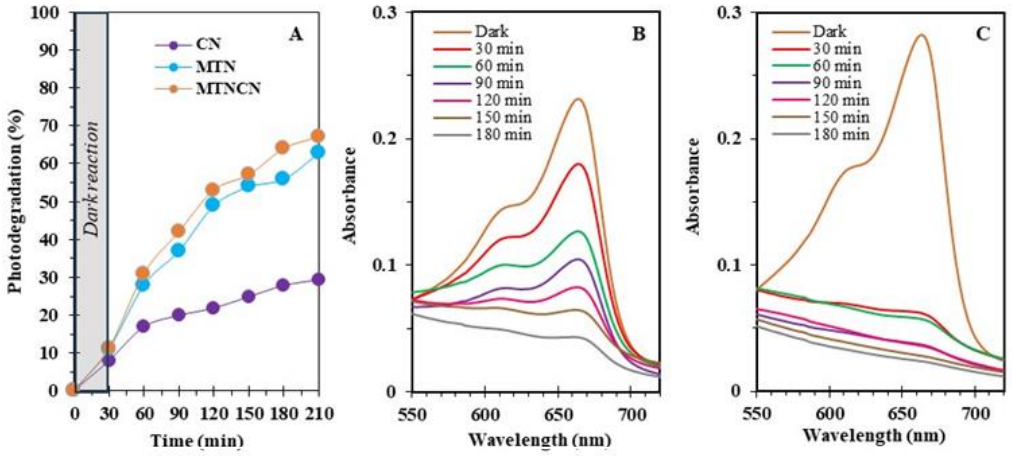


**Figure 4.** (A) Percentage degradation of MB using MTN, CN and MTNCN under UV light. Degradation of MTNCN under (B) UV and (C) solar irradiations.

Band gap energy determined from the extrapolation (at x-axis) of the graph edge form the plot of $[F(R)hv^{(0.5)}]$ versus photon energy (hv) for MTN, CN and MTNCN are about 3.04 eV, 2.74 eV and 2.94 eV, respectively. The result showed that the larger band gap energy of MTN (3.04 eV) was successfully lowered with the addition of CN probably due to a lower electron-hole recombination rate promoted by the heterojunction (CN-MTN) formed [19]. The decrease in band gap energy provides evidence of the system's enhanced ability to generate a greater number of active species for contaminant degradation over a broader light absorption region.

### 3.2 Catalytic Testing on Degradation of Methylene Blue (MB)

Figure 4 (A) shows the photocatalytic activities of the pure MTN, CN, and MTNCN in photodegradation of 100 ppm MB under UV irradiation. The first 30 minutes of reaction time, the reaction was carried out in a dark reaction

(without light irradiation) to ensure catalyst attained it adsorption-desorption equilibria. It can be seen that pure CN has the lowest activity which is only 27 % after 180 min, whereas MTN itself reaches 65.8 % of MB removal. Among all catalysts, the MTNCN sample exhibits the highest activity, showing that 67.9 % was degraded within 180 min. According to the characterization outcomes, there might have been a synergetic effect between the MTN and CN, which resulted in smaller particle size, greater surface area and a lower band gap energy. The reduction in band gap energy possibly enhances light absorption efficiency [20], thereby revealing the strong potential of MTNCN for MB photodegradation and warranting further exploration under solar irradiation.

Figure 4 shows the photodegradation of 10 ppm MB using MTNCN under (B) UV and (C) solar irradiations. MTNCN showed very high percentage of degradation under both irradiations up to 81.5 % and 97.3 %, respectively. On top of that, it was proven that better utilization of electron and hole pairs in MTNCN happen in solar irradiation. It can be clearly seen form the figures that MTNCN dramatically reduced the concentration of MB up to 78.2 % photodegradation within 30 min exposure to solar irradiation, while a much slower rate of degradation was monitored under UV light. This is because the phase junction between two different polymorphs could ease the electron transfer, thus increasing the ability to harvest the energy in solar spectrum [21]. These properties has greatly helped to shift the optical response of MTN from UV to the visible light region. Although this preliminary studies showed a significant contribution on the potential of MTNCN as a solar-driven photocatalyst in a lower concentration of MB, a detail study is worth for exploration and will be discussed in the future publication.

## 4. CONCLUSION

In conclusion, MTNCN was successfully synthesized via the impregnation method, and its photocatalytic performance was evaluated through the degradation of MB under different light sources. The structural and physicochemical properties of the catalysts were systematically characterized using XRD, FESEM–EDX, $N_2$ adsorption–desorption (BET) analysis, and UV–Vis DRS. The results confirmed the successful incorporation of CN into MTN. Moreover, MTNCN exhibited enhanced textural and optical properties, which can be attributed to the formation of a heterojunction between CN and MTN. Among all samples, MTNCN demonstrated the highest MB degradation efficiency, outperforming both MTN and CN, even under UV irradiation. Further investigation under solar light condition revealed accelerated degradation kinetics, with the most pronounced performance observed under solar irradiation, achieving 78.2 % degradation within 30 min and 97.3 % after 180 min of reaction.

## ACKNOWLEDGEMENTS

We gratefully acknowledge funding support from the Kurita Water and Environment Foundation under grant number 2023-0200-101-11 and Universiti Pendidikan Sultan Idris, Perak for the resources.

## REFERENCES

1. S. Varjani, P. Rakholiya, T. Shindhal, A.V. Shah, H.H. Ngo, J. Water Process Eng. 39 (2021) 101734.
2. K. Farhana, A.S.F. Mahamude, M.T. Mica, Materials Circular Economy, 4 (2022) 20.
3. A.P. Periyasamy, Cleaner Water, 4 (2025) 100092.
4. F. Tanos, E. Makhoul, A.A. Nada, M.F. Bekheet, E. Petit, A. Razzouk, G. Lesage, M. Cretin, M. Bechalany, Adv. Energy Sustainability Res., 5 (2024) 2400102.
5. N. Spigariol, L. Liccardo, E. Lushaj, E.R. Castellon, I.B. Martin, F. Polo, A. Vomiero, E. Cattaruzza, E. Moretti, Catalysis Today, 419 (2023) 114134.
6. M.R. Al-Mamun, S. Kader, M.S. Islam, M.Z.H. Khan, J. Environ. Chem. Eng. 7 (2019), 103248.
7. N. Farooq, P. Kallem, Z.U. Rehman, M.I. Khan, R.K. Gupta, T. Tahseen, Z. Mushtaq, N. Ejaz, A. Shanableh, Journal of King Saud University - Science 36 (2024) 103210.
8. S.M. Sidik, N.A.M. Noor, M.S. Rosmi, N.F. Jaafar, N. Hashim, M.N. Jajuli, Malaysian Journal of Microscopy, 20 (2024) 361.
9. M. Barik, D. Das, P.K. Satapathy, P. Mohapatra, Environ. Eng, Res. 28 (2023) 6.
10. M.A. Ahmed, S.A. Mahmoud, A.A. Mohamed, RSC Adv., 14 (2024) 25629-25662.
11. N.F. Jaafar, A.A. Jalil, S. Triwahyono, N. Shamsudin, RSC Adv., 5 (2019) 90991-91000.
12. X. Wang, K. Maeda, X. Chen, K. Takanabe, K. Domen, Y. Hou, X. Fu, M. Antonietti, J. Am. Chem. Soc. 131 (2009) 5.
13. Y.J. Acosta-Silva, R. Nava, V. Hernández-Morales, S.A. Macías-Sánchez, M.L. Gómez-Herrera, B. Pawelec, Appl. Catal. B: Eviron.110 (2011) 108-117.
14. N. Thankur, N. Thakur, J. Mater. Sci.: Mater. Electron, 35 (2024) 134.
15. S. Dey, S.C. Roy, Journal of Alloys and Compounds, 881 (2021) 160481.
16. W. Zhang, D. Xu, F. Wang, M. Chen, Nanoscale Adv., 3 (2021) 4370.
17. G. Ravi, N. Patra, S. Talu, Next Materials 9 (2025) 101128.
18. N. Fatemipayam, N. Keramati, M.M. Ghazi, Scientific Reports, 15 (2025) 8160.
19. R. Ghamarpoor, A. Fallah, N.E. Fard, S. Salehfekr, S. Hosseini, V. Moradi, Surfaces and Interfaces, 76 (2025) 107846.

20. T. Kobkeatthawin, J. Trakulmututa, T. Amornsakchai, P. Kajitvichyanukul, S.M. Smith, Catalysts, 12 (2022) 2.
21. M.G. Sahini, A. Parmain, I. Onoka, S.F. Mwanga, Journal of Alloys and Compounds, 1044 (2025) 183642.